Double sided arc welding of AA5182 aluminium alloy sheet

Y. Kwon and D. C. Weckman*

The feasibility and merits of using the double sided arc welding (DSAW) process for making square welds in 1·2 mm thick AA5182-O aluminium sheets in the butt-joint configuration for applications such as tailor welded blanks (TWB) has been studied. Full penetration, conduction mode DSAW welds were made using a balanced square wave AC, constant current power supply at welding speeds of 30 to 40 mm s^{-1} when using 2·1 kW welding power and between 40 and 60 mm s^{-1} when using 3·4 kW welding power. There was good cathodic cleaning of the oxide on both sides of the sheet and the weld bead quality and properties were excellent. All welds exhibited a columnar to equiaxed grain transition with up to 40% equiaxed grain area. The DSAW process was found to be capable of producing welds of equal or better quality and at comparable welding speeds to those produced using more traditional welding processes for TWB applications.

Keywords: Double sided arc welding, Aluminium, Tailor welded blanks

Introduction

Automotive manufacturers are coming under increasing regulatory pressure to improve the overall fleet mileage of their automobiles. Consequently, there is much interest in development and assessment of advanced materials and manufacturing technologies that will allow fabrication of lighter automotive bodies and structural components. For example, CO_2 laser welding of tailor welded blanks (TWB) of automotive steel sheets is a relatively new technology that has been shown to provide up to 30% weight savings for structural components.[1] Tailor welded blanks are composite blanks made from combinations of different sheet steel and galvanised coating thicknesses that are joined together along butt joints using long, full penetration square welds. Once welded, the TWB is stamped and formed into a structural component such as an inner door panel. Manufacturing of TWBs for the automotive industry requires welding processes capable of making high quality, full penetration welds between two sheets of different thicknesses at high welding speeds.[1]

Further savings in automotive body weight can be realised by making TWBs from lighter aluminium alloys such as AA5754 and AA5182 for structural components and AA6111 for outer panels;[2] however, high thermal conductivity and thermal expansion coefficient, low absorptivity and tenacious Al oxide make the welding of wrought Al alloys more challenging than the welding of traditional sheet steel alloys. To facilitate manufacturing of aluminium alloy TWBs in a high speed production environment, new welding techniques must be identified and assessed. Recent studies suggest that electron beam welding (EBW), laser beam welding (LBW) and variable polarity plasma arc welding (VPPAW) are the welding processes most likely to be successful for welding aluminium alloy TWBs.[3–4]

While multi kilowatt CO_2 laser welding of sheet steel TWBs is now a mature technology, this process is not suitable for producing TWBs in Al alloys due to the low absorptivity of Al at the 10·6 μm wavelength of the CO_2 laser. Alternatively, solid state Nd:YAG lasers are absorbed more readily by Al due to their shorter wavelength (1·06 μm).[5] The weldability of Al–Mg (5xxx series) or Al–Mg–Si (6xxx series) alloy sheet by single and dual beam CO_2 and Nd:YAG lasers in TWB applications has been examined extensively.[6–11] Weld defects such as undercutting, poor underbead quality, occluded gas porosity, hydrogen porosity and reduced weld metal strength due to loss of high vapour pressure Mg in the weld metal have been reported.[6,7,9–11] Deutsch and Punkari et al.[10,11] have recently shown that acceptable, pore free dual beam Nd:YAG laser welds with smooth under bead geometries can be produced in 1·6 mm thick AA5754 and AA5182 alloy sheet at welding speeds of 100 to 125 mm s^{-1} using total laser powers of 4·5 to 5 kW, but only when the lead laser beam power was greater than or equal to that of the lagging laser beam.

Until recently, the only arc welding process that has the potential to provide the welding rates necessary for Al alloy TWB production is the variable polarity plasma arc welding (VPPAW) process. In VPPAW, a square wave AC power supply is used to provide the necessary cathodic cleaning of the Al oxide from the weld.[4,12] The feasibility of using conduction mode VPPAW for high

Department of Mechanical and Mechatronics Engineering, University of Waterloo, Waterloo, Ontario, N2L 3G1, Canada

*Corresponding author, email dweckman@uwaterloo.ca
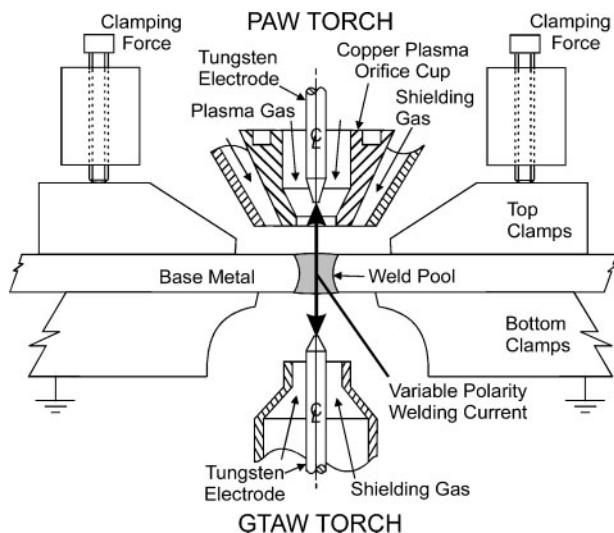
1 Schematic diagram of DSAW process and specimen clamps

speed TWB welding of 1·6 mm thick AA5182 and AA5754 Al alloy sheets has been explored by Deutsch[13] and Punkari.[14] Acceptable square welds were made in these alloy sheets at speeds up to about 50 mm s⁻¹ only when a stainless steel backing bar was used to control the under bead geometry and drop-through. However, increased power input was required because the backing bar acted as a heat sink. The under-bead oxide was not cleaned off the sheet and the weld pool was much larger than an equivalent LBW weld. Also, the VPPAW weld bead was asymmetric through the sheet thickness. This asymmetry caused undesirable angular distortion of the sheets.

The recently patented double sided arc welding (DSAW) process[15] is a relatively unique arc welding process. The DSAW process uses one power supply and two torches: frequently a plasma arc welding torch on one side of the plate and a plasma arc or gas tungsten arc welding torch on the other side as shown in Fig. 1. Special welding fixtures are required that provide access to both sides of the plate during welding. The arc is struck between the two torches. The plates to be welded are grounded and not part of the electric welding circuit. To date, the DSAW process has been used by Zhang *et al.*[15–21] to produce vertical-up, keyhole mode welds in 6 to 12 mm thick plain carbon steel, stainless steel or Al alloy plates.

The DSAW process has a number of potential advantages over existing processes such as LBW and VPPAW for aluminium tailor welded blank applications. It can provide cathodic etching of the Al oxide on both sides of the sheet, rather than just on the top side. If used in the conduction mode, the weld bead quality on both sides of the sheet can be expected to be as good as VPPAW conduction mode welds. This is beneficial to the formability and mechanical and fatigue strength of the welded blank. The weld bead would normally be symmetrical through the sheet thickness. This will significantly reduce the angular thermal distortion observed in sheets welded using the VPPAW process. Finally, the cost of a DSAW system will be a fraction of the cost of a LBW system with similar process capabilities.

The DSAW process has never before been applied to high speed welding of thin sheet such as is used in aluminium tailor welded blanks.[22] Therefore, the objectives of the present study[23] were to gain insight into the physics and operation, as well as assess the feasibility and merits of the DSAW process, as applied to welding of AA5182 aluminium alloy thin sheet in the butt joint configuration for tailor welded blanks.

Experimental

Cold rolled, 1·15 mm thick AA5182-O aluminium alloy sheet was used. The primary alloy addition in this alloy is 4·5 wt-%Mg[24] where the main role of the Mg is to provide solid solution strengthening while maintaining good ductility and formability. The alloy is considered to have good weldability.[25] All weld specimens were sheared to dimensions of 38 × 280 mm. Following Deutsch[13] and Punkari,[14] the specimens were sheared such that the weld was perpendicular to the rolling direction. This provided the best cathodic cleaning of the oxide during welding. Before welding, the specimens were degreased using acetone then the top and bottom surfaces of the specimens near the weld joint were lightly abraded with a stainless steel wire brush to break up the pre-existing oxide.[26]

The DSAW system had five main components: a variable polarity power supply and plasma arc welding console, a PAW torch, a GTAW torch, a welding table traversing mechanism for holding and moving the weld specimens between the two fixed torches at the desired welding speed and a PC microcomputer based control and data acquisition system. A Thermal Arc WC100B PAW welding torch and Thermal Dynamics, Thermal Arc WC 100B plasma console were used because the PAW pilot arc facilitated initiation of the welding arc between the two torches. As shown in Fig. 1, the PAW torch was mounted above the weld specimens in a fixed position. A WELDCRAFT model WP-27 GTAW torch was mounted in a fixed position underneath the weld specimens. A Miller Aerowave AC/DC power supply was used and operated in the constant current, square wave AC mode at a frequency of 60 Hz. The PAW torch was connected via the plasma console to the positive terminal of the power supply and the GTA torch was connected to the negative terminal.

The top and bottom clamps shown in Fig. 1 were used to hold the two sheet weld specimens in the butt joint configuration while they were moved on a carriage between the PAW and GTAW torches at the welding speed. The weld specimens and carriage were grounded and not part of the arc welding circuit. During welding, the welding current flowed from one torch electrode, through the sheets to the opposite torch electrode creating two welding arcs, one acting on the top surface and the other acting on the bottom surface of the weld seam simultaneously during welding.

A PC microcomputer and LabView 6·0 based data acquisition and control software was used to measure the welding current and voltage, and to control the travel speed of the specimen carriage. The variable polarity welding current was measured using a LEM LT505-S Hall-effect current transducer and the voltage was measured using a LEM LV100 Hall-effect voltage transducer. These current and voltage signals were passed through a low pass filter with a 10 kHz cut off
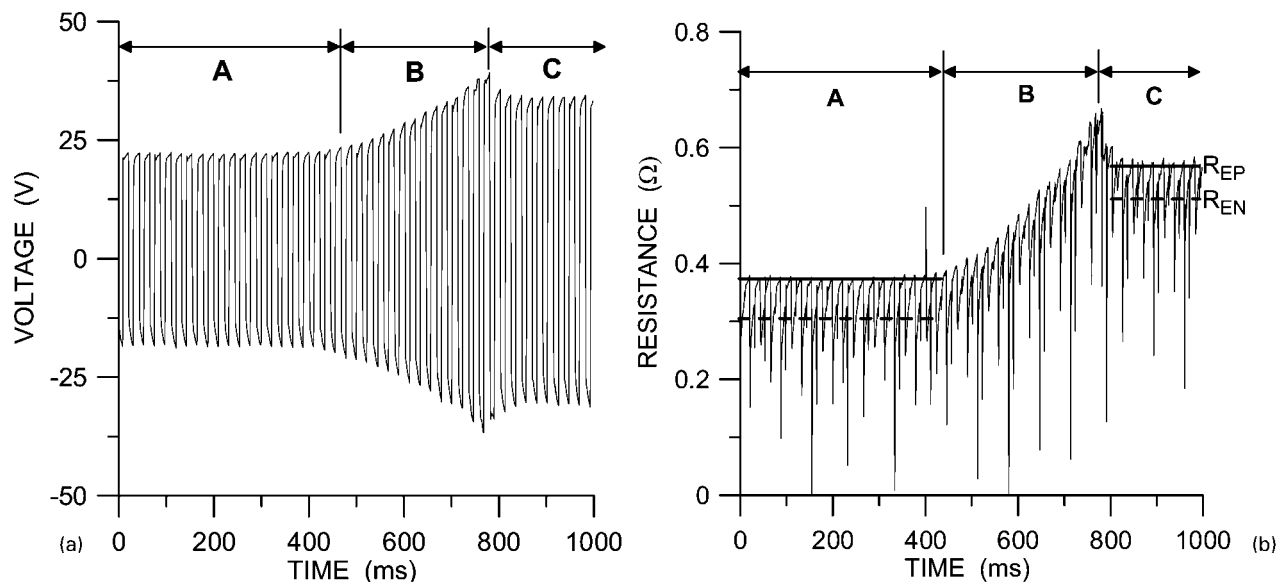
a arc voltage; *b* arc resistance
2 Measured arc voltage and resistance versus time at beginning of DSAW weld

to protect the data acquisition from damage from high frequency transmissions from the power supply inverter and the pilot arc starter. The data sample rate was 1000 samples per second. The acquired current and voltage data were used to calculate root mean square (RMS) values of current, voltage, arc resistance and power.

A number of preset independent weld process parameters were established through an initial set of trial welding experiments.[23] For example, the best cathodic cleaning on both the top and bottom surface of the DSAW welds was realised when a balanced, symmetrical, square wave form was used, i.e. peak currents in electrode negative and positive were set equal and the time spent in electrode negative and positive were set equal. All other preset PAW and GTAW torch parameters used for subsequent experiments are given in Table 1.

Before each weld, the PAW pilot arc was started and then a free standing arc of the desired peak welding current was created directly between the PAW and GTAW torches. Double sided arc welds were then made by moving the weld specimens between the fixed torches at the desired welding speed. Conduction mode DSAW welds were made at welding speeds ranging from 10 to 90 mm s^{-1} and total RMS welding powers ranging from 1·8 to 3·4 kW where the welding power was varied by changing the peak current. Video imaging of the DSAW welds was performed using a LaserStrobe video imaging

system operated at 30 frames per second.[27] This system allowed video imaging of the DSAW with partial or complete attenuation of the light emitted by the welding arc.

Metallographic examination of polished and etched specimens was performed using an OLYMPUS optical microscope with an IMAGE-PRO 4·5 image analysis system. Two different reagents were used to etch the specimens, i.e. Keller's reagent was used to reveal the solidification microstructure while Beck's reagent was used to reveal the grain structure.[28] Top weld width, bottom weld width, undercut, drop-through, weld area and equiaxed grain area of each weld were measured. Mechanical properties were evaluated using Vickers microhardness tests and ASTM A370 tensile tests transverse to the welds.

The melting ratio, *MR*, was calculated for each weld to determine the effects of welding process conditions on the overall energy coupling efficiency. The melting ratio is the fraction of the total incident power which is used to heat and melt the weld metal. The equation used to calculate *MR* is[29]

$$MR = \frac{\left[\rho C_p \left(T_{mp} - T_o\right) + \Delta H_f\right] L_w A_w}{L_w \left(\frac{P_L}{v_{ws}}\right)} \qquad (1)$$

where L_w is the length of weld metal, A_w is the weld metal area, ρ is density, C_P is the specific heat, ΔH_f is the latent heat of fusion, v_{ws} is welding speed, T_{mp} is the solidus temperature, T_0 is room temperature and P_L is the power from the power supply. The thermophysical properties of A5182 used for this calculation were $\rho = 2 \cdot 65$ Mg m^{-3}, $C_p = 0 \cdot 904$ kJ kg^{-1} K^{-1}, $\Delta H_f = 397$ kJ kg^{-1} and $T_{mp} = 850$ K.[24]

Results and discussion

Initial transients

Arc coupling between the torches and the aluminium sheets at the beginning of a DSAW weld was not immediate; rather, there was an initial transient at the leading edge of the sheets. Figure 2*a* shows the welding

Table 1 Preset welding parameters used for PAW and GTAW torches

Torch parameter	PAW	GTAW
Arc gap, mm	6·25	5·0
Orifice diameter, mm	3·2	–
Plasma gas	UHP Ar	–
Plasma gas flowrate, L min^{-1}	0·45	–
Shielding gas	UHP Ar	Ar
Shielding gas flowrate, L min^{-1}	19	30
Electrode composition	W–1%Zr	W–1%Zr
Electrode diameter, mm	4·8	3·2
Electrode angle, °	20	60
Electrode truncation, mm	1·0	0·3
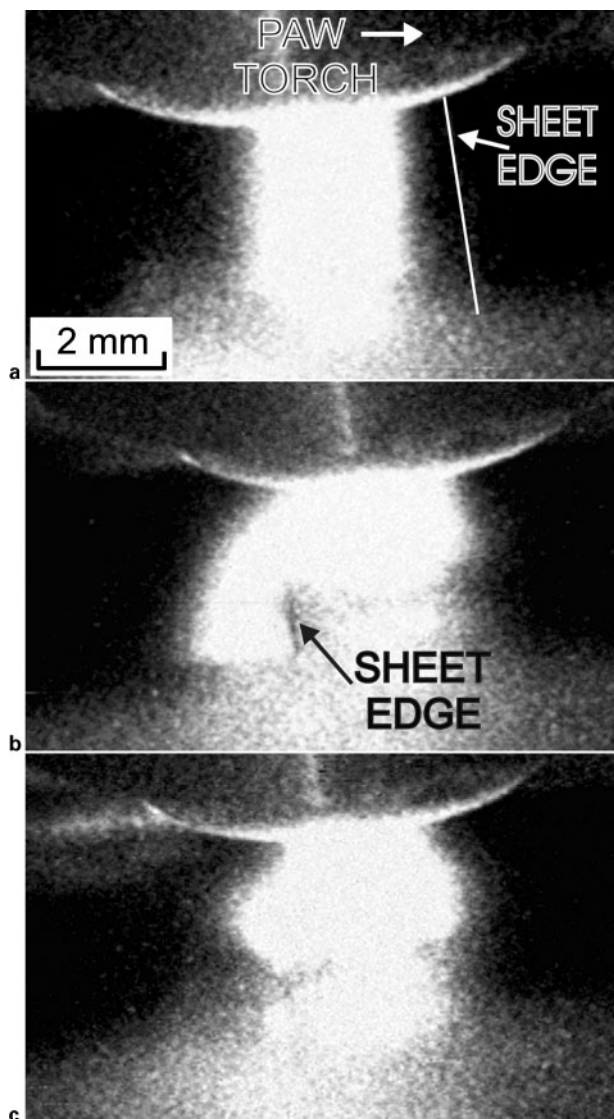
a free standing arc between two torches; *b* arc wrapping around leading edge of workpiece and elongating; *c* arc finally couples with sheets and starts to melt workpiece

3 LaserStrobe video images of PAW arc during initial start-up transient

voltage versus time at the beginning of a DSAW weld made using a peak welding current of 60 A. During stage A, there was a free standing arc between the two torch electrodes as shown in the LaserStrobe image in Fig. 3*a*. The measured peak voltages were ~20 V. During stage B, the weld specimens began to advance between the two torches at the welding speed as shown in Fig. 3*b*. There was a gradual increase in the peak voltages until the arc voltage reached maximum peak voltages of about 39 V (*see* Fig. 2*a*). This increase in voltage was due to the increase in arc length as the arc travelled from one electrode around the edge of the advancing weld specimens to the second electrode without passing through the weld specimens (*see* Fig. 3*b*). Finally, in Stage C, the arc length and resistance became excessive and the arc coupled directly with the sheets creating separate PAW and GTAW arcs above and below the sheets. The total welding current passing directly through the sheets is shown in Fig. 3*c*. At this point, the workpiece started to heat and to melt.

With arc coupling, the length of the arc was shortened resulting in decreased peak voltages until it stabilised at ~32 V (*see* Fig. 2*a*). The voltage in Stage C is 12 V greater than in Stage A due to the addition of potential drops across the newly created cathode and anode fall regions adjacent to the top and bottom sheet surfaces and the small voltage drop across the weld specimens due to the resistivity of the molten metal in the weld pool.

Figure 2*b* shows a plot of the calculated resistance between the two electrodes versus time. The resistance was calculated using the measured current and voltage data and Ohm's law, i.e. $R = V/I$. The resistance fluctuates in a manner similar to the arc voltage during the initial start-up transient of the DSAW weld. In stage A (free standing arc), the arc resistances were $R_{EP} \approx 0.37\ \Omega$ and $R_{EN} \approx 0.30\ \Omega$ where electrode positive, EP, is with respect to the PAW electrode. The slight differences in total arc resistances, R_{EP} and R_{EN}, are thought to be due to differences in electrode and arc temperatures of the PAW and GTAW torches as they switched from straight to reverse polarity. During Stage B, the arc resistance increased steadily to a maximum of ~0.68 Ω as the arc wrapped around the leading edge of the specimens (*see* Fig. 3*b*). Finally, during Stage C, the arc coupled with the sheet surfaces and the arc resistance dropped to ~0.57 Ω. The arc resistance during Stage C is greater than the free standing arc in Stage A due to the additional resistance introduced by the cathode and anode fall regions on the surface of the plate and the small resistance of the specimens. Transients were again observed at the end of the weld. These transients in arc coupling resulted in lack of fusion for the first and last 10 mm of the weld joint. Thus, start-up and run-off tabs may be required in applications where a full length DSAW weld is required between the two sheets.

Effects of welding speed and power on weld geometry

Figure 4 shows the bottom surface of DSAW welds produced using 3·4 kW welding power and welding speeds from 30 to 70 mm s^{-1}. The top surfaces of these welds were very similar in appearance. At the slowest welding speed, the weld width was greatest and blowholes occurred (*see* Fig. 4*a*). Blowhole defects were observed periodically along the DSAW weld beads when the energy input per unit length was too large, i.e. either the power input was excessive and arc forces were sufficient to blow a hole through the weld pool, or the welding speed was too slow and the weld width and weld pool were too large relative to the sheet thickness. In the latter case, surface tension forces were not sufficient to support the weight of the large weld pool and resist the arc forces. Note that immediately following the blowhole, there was typically about 5 to 10 mm of unwelded sheet and then arc coupling would re-establish and welding resume.

As shown in Fig. 5, transients in the arc voltage were observed when blowholes were produced. When the blowhole occurred, the arc voltage dropped suddenly from ±37 to ±25 V. This was the same as the initial free standing arc voltage and an indication that the arc was passing from the PAW torch directly to the GTAW torch through the blowhole without coupling to the sheet. Following this, the arc voltage increased until a
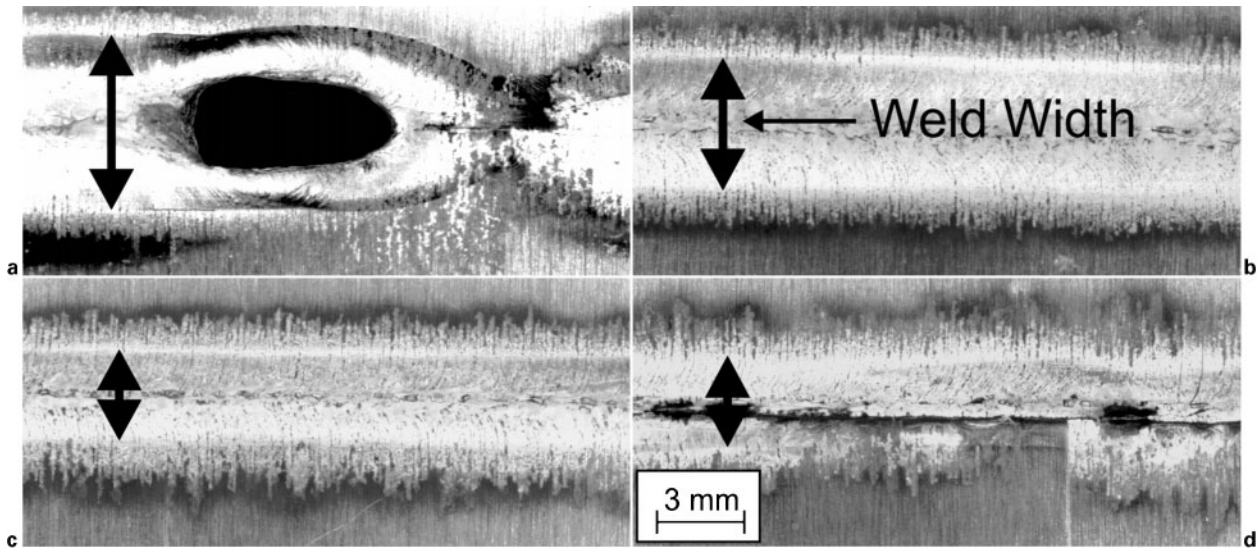
a 30 mm s^{-1} with blowhole; *b* good but wide weld at 40 mm s^{-1}; *c* good weld at 60 mm s^{-1}; *d* inconsistent arc coupling and fusion at 70 mm s^{-1}

4 Bottom surface of welds made using constant welding power of 3·4 kW and different welding speeds

peak voltage of 43 V was reached. Finally, the arc length became excessive and coupling between the arc and the sheet was re-established and welding resumed. The calculated arc resistance mirrored this behaviour. Fluctuations in the voltage that occur whenever a blowhole is produced may be used beneficially in a production welding system to indicate in real time that a blowhole weld defect has occurred.

As may be seen in Fig. 4*b* and *c*, very good weld bead geometries with excellent cathodic cleaning of the oxide and no evidence of undercutting were produced at welding speeds of 40 to 60 mm s^{-1}. The weld produced at 40 mm s^{-1} (Fig. 4*b*) was considered to be acceptable, but oversized, due to its large weld width/sheet thickness ratio. Cathodic cleaning of the oxide became less effective as the welding speed increased. Finally, welds produced at welding speeds over 70 mm s^{-1} (Fig. 4*d*) were considered unacceptable due to inconsistent arc

coupling, cathodic cleaning of the oxide and fusion along the weld bead (*see* Fig. 4*d*).

Figure 6 shows transverse sections of the welds shown in Fig. 4*b*, *c* and *d*. As expected, weld widths decrease with increasing welding speed. Weld bead geometries are very good with some underfill and drop-through, which decreased as the weld speed increased and the weld width decreased. Also, unlike the non-symmetric, V-groove weld geometry typical of VPPAW welds produced by Deutsch[13] and Punkari[14] in these same alloy sheets, all of the good DSAW conduction mode welds produced in the present study were symmetric, full penetration welds with straight or slight hour glass shaped fusion boundaries, similar to the desirable weld
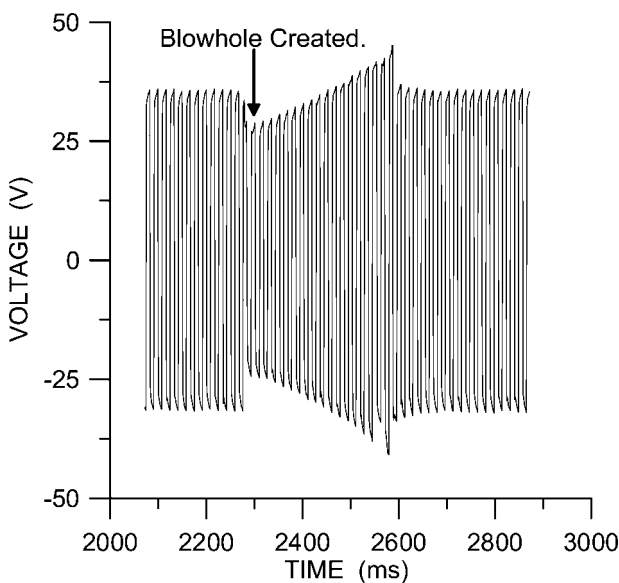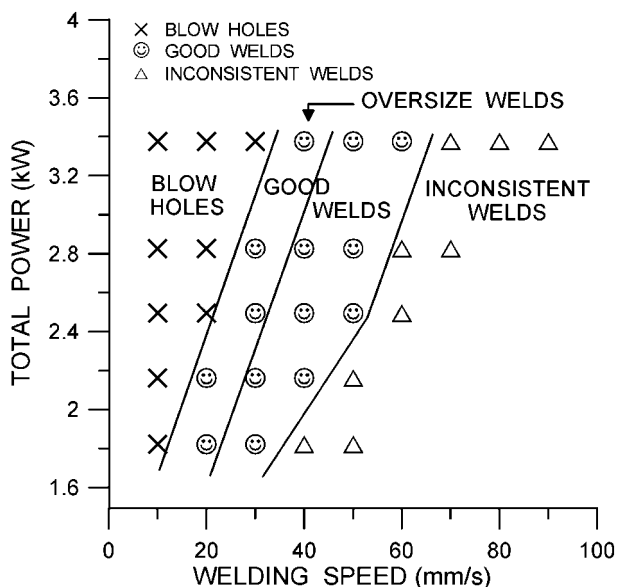

5 Measured arc voltage versus time during creation of blowhole in DSAW weld
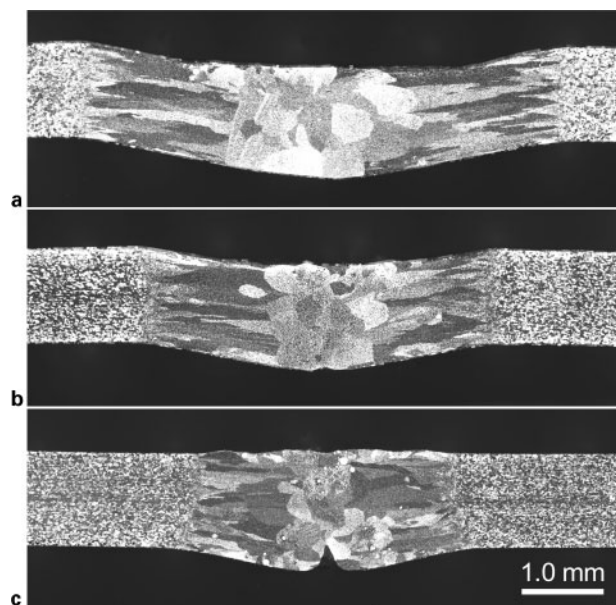
a good but wide weld at 40 mm s^{-1}; *b* good weld at 60 mm s^{-1}; *c* narrow weld with lack of fusion and hydrogen pores at 70 mm s^{-1}

6 Transverse sections of DSAW welds made using welding power of 3·4 kW and different welding speeds

7 Quality of DSAW welds versus welding speed and total power

bead geometry typically produced by LBW keyhole mode welding.[10–14]

In the DSAW welds shown in Fig. 6, columnar grains have grown from the fusion boundary towards the centre of the welds where there is a transition from columnar to equiaxed grains. The weld shown in Fig. 6c, made at 70 mm s^{-1}, had intermittent arc coupling and cathodic cleaning of the oxide. Where this occurred, there was significantly reduced energy input into the base metal (BM) and incomplete melting and fusion (see Fig. 4d). There was also an increased propensity for hydrogen porosity in the welds produced with intermittent arc coupling as evidenced by the small white circles in the weld metal in Fig. 6c.

Figure 7 shows a process map giving qualitative assessments of the weld bead appearance versus welding speed and total welding power used. Blowholes occurred at the slowest welding speeds. As the welding speed was increased, the DSAW welds changed first to oversized, but good welds and then to good welds. Unacceptable welds with inconsistent arc coupling and cathodic cleaning of the oxide were produced at the highest welding speeds. The boundaries between all regimes moved towards higher welding speeds as the total power was increased. The highest welding speed at which good welds were produced was 60 mm s^{-1} when using 3·4 kW welding power. This is greater than the 50 mm s^{-1} maximum welding speed attained by Deutsch[13] using VPPAW to weld this same aluminium alloy sheet. It is about half the optimal welding speeds of 100 to 125 mm s^{-1} reported by Deutsch *et al.*[10] when welding this alloy sheet using a dual beam Nd:YAG welding system.

Figure 8a shows weld width versus welding speed for two different welding powers. The top and bottom weld widths are almost the same at a given welding speed for both power levels. This is further indication that these welds were fully two-dimensional (2D) with straight fusion boundaries through the sheets (see Fig. 6). When using 2·1 kW welding power, the weld width decreased rapidly from 7·5 to 2·7 mm as the welding speed increased from 20 to 50 mm s^{-1}. At a welding speed
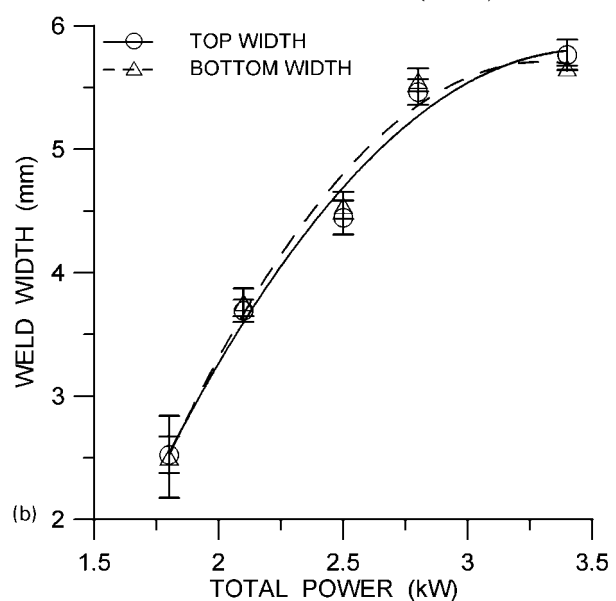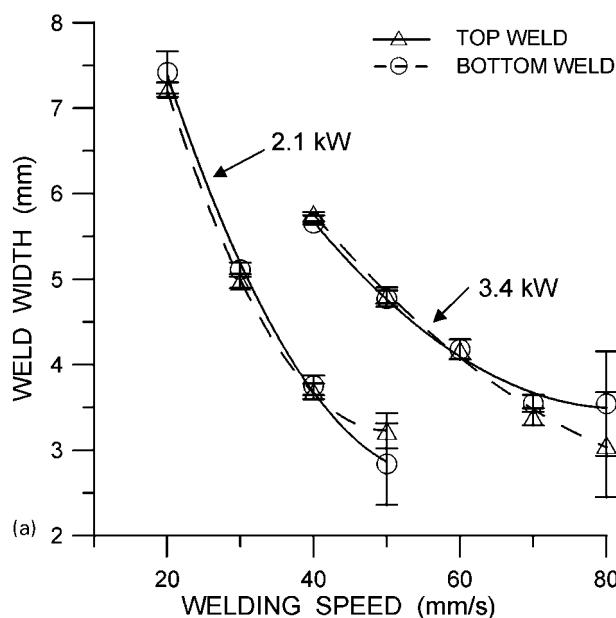
8 Top and bottom weld width versus *a* welding speed when using 2·1 and 3·4 kW welding powers and *b* welding power at welding speed of 40 mm s^{-1}

of 20 mm s^{-1}, the weld width was very large compared to the thickness of the specimen (1·15 mm). This was labelled as an oversized, good weld in Fig. 7. The increased variance of weld width data at the highest welding speed (50 mm s^{-1}) was due to inconsistent arc coupling. The width of the welds produced using 3·4 kW welding power were greater than those produced at 2·1 kW. Again, weld widths decreased to ~3·4 mm with increased welding speed and the increased variance in the data at the highest welding speed of 80 mm s^{-1} was evidence of inconsistent arc coupling.

The effect of total welding power on weld dimensions at a fixed welding speed of 40 mm s^{-1} is shown in Fig. 8b. When the total power was 1·8 kW, the weld widths were small (~2·5 mm) and inconsistent cathodic cleaning and arc coupling occurred resulting in welds such as those shown in Fig. 4d. As the power increased, the heat input per unit distance increased leading to good cathodic cleaning and larger welds. For an increase
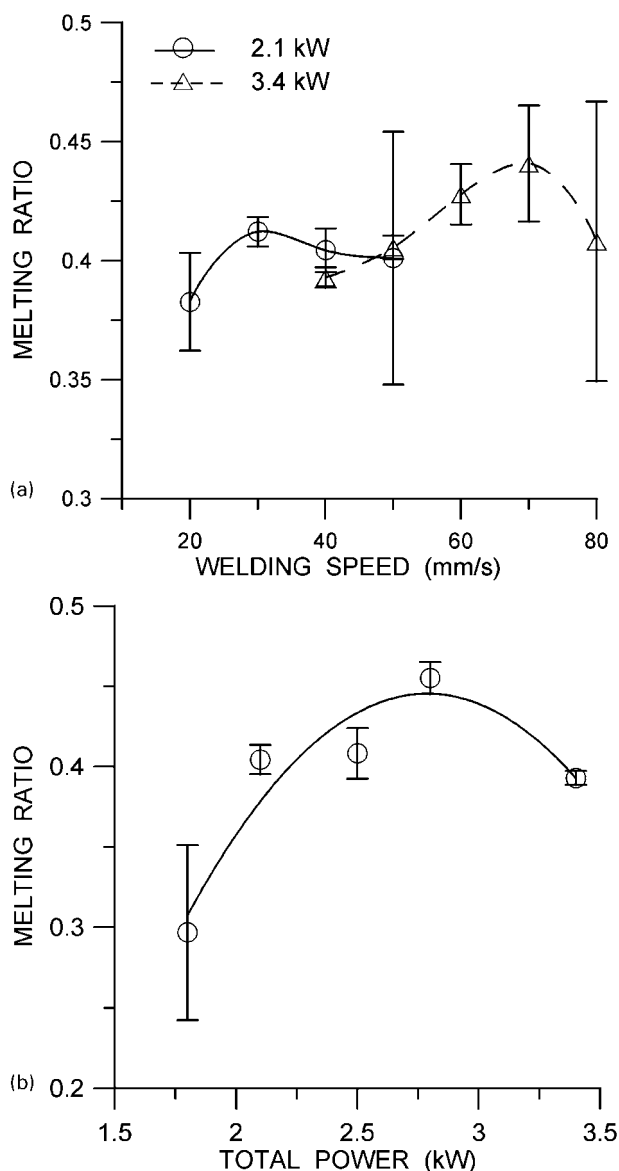
9 **Melting ratio versus *a* welding speed when using 2·1 and 3·4 kW welding powers and *b* welding power at welding speed of 40 mm s⁻¹**

from 1·8 to 2·7 kW, there was a linear increase in weld width. This behaviour is consistent with that predicted by Rosenthal's 2D analytical solution.[30,31] However, there was little change in weld width when the welding power was increased further to 3·4 kW, because the welds were so large relative to the distance between the clamps (*see* Fig. 1) that the clamps started to act as significant heat sinks. This limited further increase in weld width with increased welding power. The measured weld areas of these welds exhibited the same trends as the weld widths, because the DSAW welds were full penetration and essentially 2D in shape (*see* Fig. 6).

Figure 9 shows plots of the melting ratio versus welding speed and welding power. A higher melting ratio was observed for a total power of 3·4 kW than for a power of 2·1 kW. When using 2·1 kW, the melting ratio increased from 0·38 to a maximum value of 0·41 as speed increased from 20 to 30 mm s⁻¹. This is because the time available for heat conduction into the heat affected zone (HAZ) or the environment decreases as welding speed increases. However, as the welding speed

increased beyond 30 mm s⁻¹, the melting ratio variations increased and the average value decreased to 0·4. This decrease was accompanied by incomplete oxide cleaning and intermittent coupling between the arc and the sheet. A similar trend is observed for a total power of 3·4 kW, except that a higher maximum melting ratio of 0·43 occurred at a higher welding speed of 70 mm s⁻¹.

Figure 9*b* shows the melting ratio versus total welding power at a welding speed of 40 mm s⁻¹. The melting ratio increased as welding power was increased up to 2·8 kW. For higher power, the melting ratio decreased. At the lowest welding power of 1·8 kW, the melting ratio was only 0·3 and the scatter in the values is high because of inconsistent arc coupling and cathodic cleaning. As the power increased, cathodic cleaning improved, good welds were produced and the melting ratio increased to a maximum value of 0·45 at 2·8 kW. This is very close to the theoretical maximum value of 0·48 predicted by Swift-Hook and Gick[29] for 2D keyhole mode laser beam welds. When the welding power exceeded 2·8 kW, the melting ratio decreased from 0·45 to 0·38 as the weld pool became large enough that significant heat was lost to the clamps by conduction, limiting the weld width and decreasing the melting ratio. This behaviour was also observed in the research of Fuerschbach and Knorovsky[32] who used a calorimetric technique to study the melting efficiency of PAW and GTAW welding of 304 stainless steel and Ni 200 specimens. They reported that the melting efficiency of PAW and GTAW welds was 0·46 at the highest welding speeds but decreased to 0·15 at slower speeds as more heat was lost to the clamps by conduction.

The DSAW process efficiency is much better than either the LBW or VPPAW processes when used to weld this aluminium alloy sheet. Punkari[11,14] and Deutsch *et al.*[10,13] found that the maximum melting ratio of single beam Nd : YAG laser welded AA5182 alloy sheet was ∼0·3 and was only 0·2 for dual beam laser welds. They suggested that these values were lower than the theoretical value of 0·4, because a large portion of the incident laser beam was reflected out the top of the weld or passed through the keyhole and sheet and was not absorbed by the BM. Punkari[14] and Deutsch[13] found that the maximum melting ratios of VPPAW welds was only 0·2. This value was observed in full penetration welds which were in direct contact with the stainless steel backing bar. This bar acted as a heat sink and prevented increase in the melting ratio above 0·2.

Figure 10 shows graphs of measured underfill and drop-through versus welding speed for DSAW welds produced using 2·1 and 3·4 kW welding power. Underfill is the distance from the top surface of the sheet to the lowest point on the top surface of the weld bead and drop-through is the amount that the weld bead metal sags below the sheet. Drop-through was always larger than the underfill; however, it never exceeded 50% of the sheet thickness. These phenomena occur because the weld pool is held in place by surface tension on the top and bottom weld pool surfaces during welding. Gravity and arc forces from the plasma and shielding gases acting on these free surfaces cause the weld pool to sag below the sheet surface. At a fixed power, drop-through and underfill decreased with increasing welding speed (*see* Fig. 10*a*), because the width, volume and therefore total weight of weld metal decrease as the
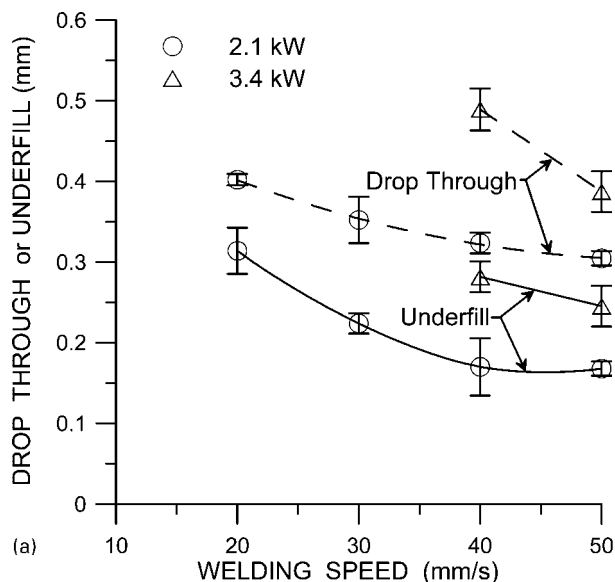
(a)
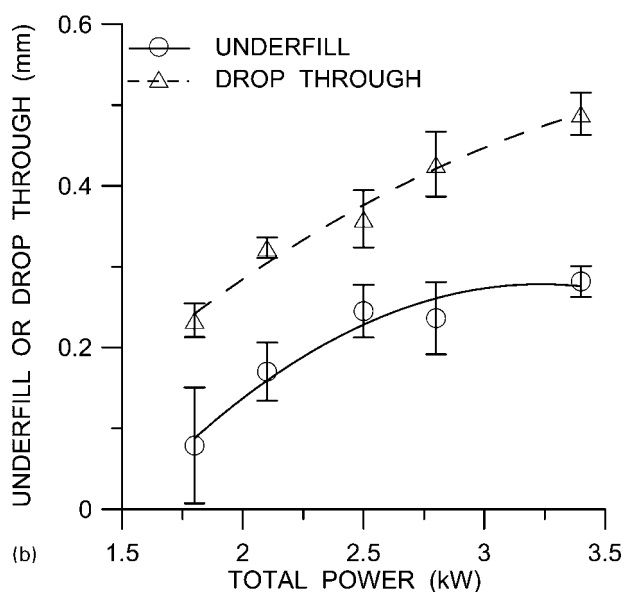
(b)

10 Effects of welding speed on weld bead drop-through and underfill when using total welding powers of 2·1 and 3·4 kW *a* versus welding speed and *b* versus welding power at 40 mm s^{-1} welding speed

welding speed increases. Figure 10*b* shows the effect of welding power on underfill and drop-through at a welding speed of 40 mm s^{-1}. Both underfill and drop-through increase with increased welding power, because larger weld pools are produced as the power increases.
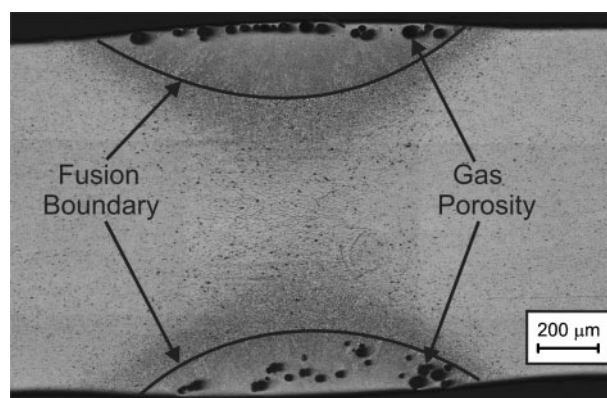
Hydrogen porosity

Porosity in aluminium welds is generally known to be produced by hydrogen that is readily absorbed into molten aluminium during welding.[25,33] Hydrogen may be introduced from water adsorbed on the BM surface, from the hydrated oxide on the specimen surface or from moisture in the shielding gas.[25,26,33] As aluminium weld metal solidifies, any absorbed hydrogen is rejected from the solid into the liquid metal at the solid/liquid interface leading to nucleation and growth of hydrogen gas bubbles in the liquid. These bubbles will naturally try to float to the surface of the weld pool and escape into the atmosphere; however, if the weld solidifies before the hydrogen can escape or the oxide has not
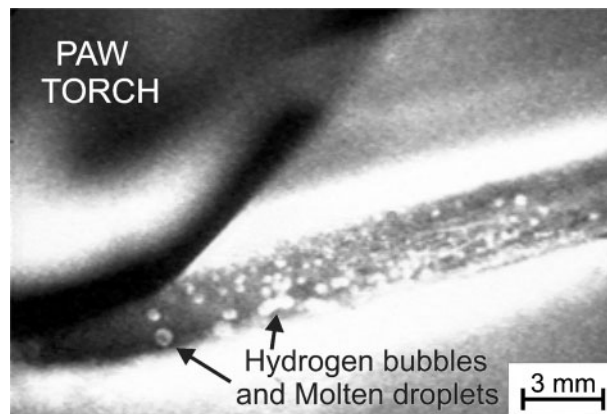
11 LaserStrobe video image of hydrogen gas bubbles breaking through top weld pool surface and small molten droplets ejected from top weld pool during DSA welding of 1·15 mm thick AA 5182 aluminium sheet
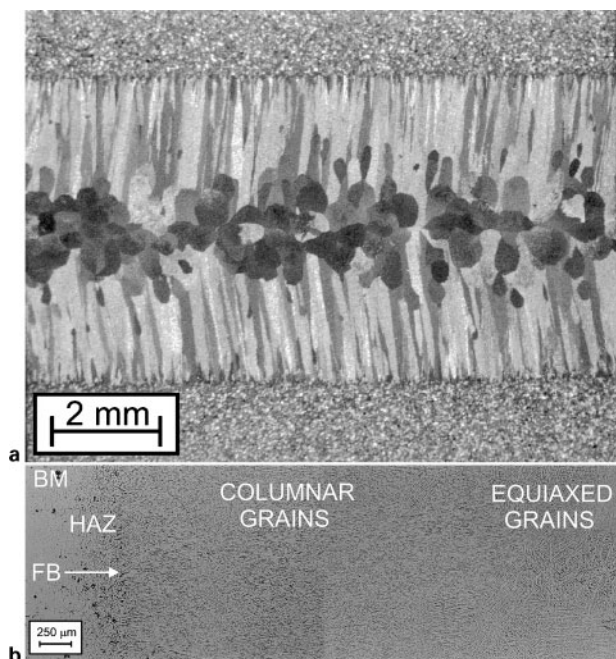
been completely removed from the weld pool surface, then hydrogen is trapped in the weld and gas pores are formed. Bailey and Pilkey[34] have shown that even small amounts of porosity in Al TWBs reduces the strain to failure or formability of the welded blank by as much as 20%, as the onset of localisation and failure was always predicted to occur at pores.

Direct evidence of hydrogen gas bubbles bursting through the top surface of a DSAW weld pool and in some cases ejecting small molten droplets of aluminium into the air above the weld pool surface during welding is shown in the LaserStrobe video image of Fig. 11. A transverse section of partial penetration DSAW welds made on as received 2·5 mm thick AA5182 aluminium sheet is shown in Fig. 12. The sheet was degreased but not wire brushed prior to welding. There are many hydrogen gas bubbles trapped in both the top and bottom welds. This suggests that the pre-existing oxide on the sheet surfaces were a significant source of hydrogen and that cathodic etching of the oxide during welding was not sufficient to prevent hydrogen absorption into the weld pool. The hydrogen gas bubbles formed in the bottom weld could not float up and out of the surface of the weld and were trapped in the bottom weld. On the other hand, hydrogen gas pores that formed in the top weld were able to float to the surface

12 Transverse section of partial penetration DSAW welds made in 2·5 mm thick AA 5182 aluminium sheet exhibiting hydrogen porosity

14 **Percentage equiaxed grains area versus welding speed for DSAW welds using power of 2·1 and 3·4 kW**

a polished and etched top surface; *b* transverse section showing solidification microstructure

13 **Macrostructure of AA5182 alloy DSAW weld in 1·15 mm thick sheet made at 40 mm s^{-1} using 3·4 kW power showing columnar grains from fusion boundary toward centre of weld and equiaxed grains at centre of weld**

of the top weld, but were not able to escape through this surface due to incomplete cathodic cleaning of the oxide film and were, therefore, trapped in the weld just below the surface. As shown in Fig. 6a and b, hydrogen porosity was significantly reduced in the DSAW welds when the pre-existing oxide was removed by wire brushing before welding and the welds were full penetration. Any hydrogen bubbles that form in full penetration DSAW welds are free to float to the top surface of the weld pool and escape during welding as shown in Fig. 11.

Columnar to equiaxed grain transition in DSAW welds

Figure 6 shows transverse sections of DSAW welds produced at 40, 60 and 70 mm s^{-1} respectively, while Fig. 13a shows the polished and etched surface of the weld produced at 40 mm s^{-1}. Beck's Reagent[28] was used to reveal the grain structure. In all cases, columnar grains initially grew toward the centre of the DSAW welds by epitaixial growth of the BM grains at the fusion boundary (FB). In Fig. 13b, Keller's Reagent was used in the transverse section of the same weld to reveal the solidification microstructure. The solidification microstructure in the columnar grains was cellular–dendritic. However, towards the centre of the weld, continued growth of the columnar grains was blocked by nucleation and growth of large equiaxed–dendritic grains at the centre and tail of the weld pool.

The transition from columnar to equiaxed grains in fusion welds as shown in Figs. 6 and 13 is known to be beneficial in preventing solidification and centreline cracking in welds[33,35] and improving the mechanical properties of the weld metal such as strength, toughness and ductility.[33,36] A columnar to equiaxed grain
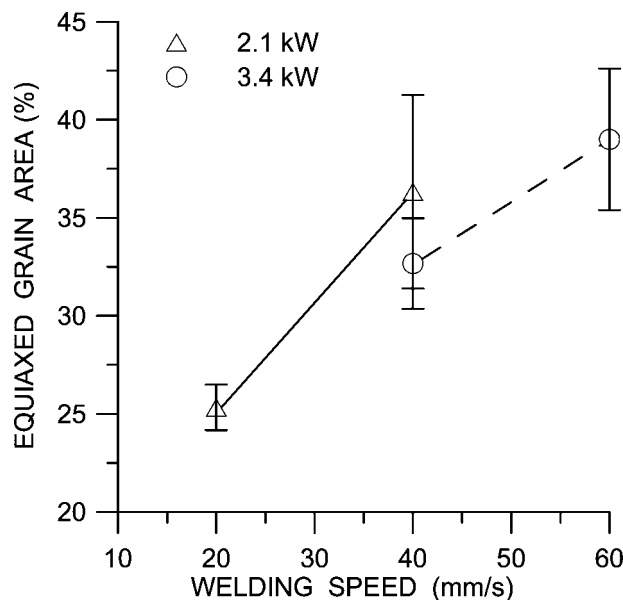
transition may be promoted in aluminium alloy welds by providing first a supply of embryos from which equiaxed grains may grow and second thermal conditions at the fusion boundary which favour the nucleation and growth of these embryos into equiaxed grains.[33,35,37–40] The most common source of embryos in commercial alloys is heterogeneous nucleation from residual TiB$_2$ inoculants added during the initial casting of commercial alloys.[41] The photomicrographs in Figs. 6 and 13 suggest that there was sufficient residual TiB$_2$ in the A5182 alloy sheet to provide some heterogeneous nucleation sites for equiaxed grains, but not enough to promote a 100% equiaxed grain structure.

With a sufficient supply of embryos, the welding process parameters, especially high welding power and welding speed combinations,[33,35,37–40] will also influence the percentage equiaxed grains produced in aluminium welds. Figure 14 is a plot of the percentage equiaxed grain area in DSAW welds versus welding speed for welding powers of 2·1 and 3·4 kW. At both welding powers, as the welding speed increased, the percent equiaxed grain areas increased from 25 to about 38 %. This trend is consistent with experimentally measured and modelled behaviour in a wide range of aluminium alloys.[33,35,37–40] However, at a constant welding speed of 40 mm s^{-1}, as the welding power was increased from 2·1 to 3·4 kW, the percentage equiaxed grain area decreased. This behaviour is opposite to previously reported experimental results and model predictions of the effect of weld power on percentage equiaxed grain area.[33,35,37–40] Whereas increased welding power normally causes a proportional increase in weld size and decrease in thermal gradient, it was previously noted that the weld width of welds produced using 3·4 kW welding power was limited by the relatively close proximity of the clamps (*see* Fig. 8) which act as chills. This would result in smaller than expected welds and higher than expected thermal gradients in the liquid at the fusion boundary which in turn would cause a decrease in the extent of the zone of undercooling required for nucleation and growth of equiaxed grains at

the tail of the weld and a reduction in the percentage equiaxed grain area as is observed.

Mechanical properties of DSAW welds

There were no significant changes in hardness of the AA5182-O BM, HAZ and weld metal. The measured hardness ranged between 73 and 78 VHN. While Pastor *et al.*[9] have reported a measurable decrease in strength and hardness of keyhole mode laser welds made in this alloy due to loss of Mg in the weld metal during welding, EDX analysis of the DSAW welds made in the present study revealed no measureable change in the Mg content of the DSAW welds. This is consistent with the microhardness results.

All tensile test weld specimens failed in the weld metal. The yield strength of the DSAW welded AA5182 aluminium sheets were $\sim 5\%$ lower than those of the unwelded AA5182 aluminium sheet, i.e. 120 ± 2.6 MPa versus 126 ± 2.5 MPa, whereas the ultimate tensile strength of the welded specimens was about 8% lower, i.e. 258 ± 2.0 MPa versus 283 ± 1.2 MPa. This represents an overall joint efficiency of 91%.

Conclusions

The weldability of 1.2 mm thick AA5182-O aluminium alloy sheet in the butt joint configuration using a new and novel DSAW process has been assessed. Full penetration conduction mode welds were made using a square wave AC, constant current power supply connected to a PAW welding torch above the weld specimens and a GTA welding torch below the weld specimens. Good quality DSAW welds could be produced in this material with excellent cathodic cleaning of the oxide from both the top and bottom surfaces of the weld bead at welding speeds from ~ 30 mm s^{-1} when using 1.8 kW welding power to ~ 60 mm s^{-1} when using 3.4 kW welding power. The weld width, weld area and weld bead underfill and drop-through were found to decrease with increased welding speed whereas they increased with increased welding power.

The melting ratio of this conduction mode DSAW process was found to increase to a maximum value of ~ 0.45 with increasing welding speed to 70 mm s^{-1}. This is very close to the maximum theoretical melting ratio of 0.48. In addition, the maximum DSAW melting ratio is almost double the melting ratio values reported for welding these same alloys using single and dual beam Nd : YAG laser welding and VPPAW welding.

Some hydrogen porosity was observed in the weld metal especially in partial penetration welds where the hydrogen bubbles could not float up and out of the bottom weld pool or could not break through a residual oxide film left due to incomplete cathodic cleaning of the surface oxide during welding. However, hydrogen porosity was significantly reduced in the full penetration DSAW welds because the hydrogen bubbles were able to escape through the oxide free top surface during welding.

All DSAW welds exhibited a columnar to equiaxed grain transition with percentage equiaxed grains ranging from 25 to 40%. The percentage equiaxed grain area was found to increase with increased welding speed and the highest percentage equiaxed grain area was observed with the highest welding current and power combination. In addition, mechanical properties of the AA5182-O aluminium alloy sheet were not strongly affected by the DSAW process. The overall joint efficiency of these DSAW welds was 91%.

The DSAW process has never before been applied to high speed welding of thin sheet such as is used in aluminium alloy tailor welded blanks. It has a number of potential advantages over existing processes such as Nd : YAG laser beam welding and variable polarity plasma arc welding. The DSAW process has been shown to provide cathodic etching of the aluminium oxide on both sides of the sheet, rather than just on the top side. The weld bead quality is as good as that possible on the top weld bead only of VPPAW welds. This is beneficial to the formability and mechanical and fatigue strength of the welded blank. The weld bead is normally symmetrical through the sheet thickness. This can be expected to reduce the angular thermal distortion of the sheets which was observed in sheets welded using the VPPAW process. The significant potential advantages of the DSAW process with respect to the welding of tailor welded aluminium alloy blanks may make DSAW the process of choice for such applications.

Acknowledgements

References

1. E. Kubel: *Manufact. Eng.*, 1997, **119**, (5), 38–45.
2. R. J. Kazmier: *Adv. Mater. Process.*, 2001, **94**, (1), 42–44.
3. S. Das: *Adv. Mater. Process.*, 2000, **157**, (3), 41–42.
4. E. Craig: *Weld. J.*, 1998, **67**, (2), 19–25.
5. W. W. Duley: 'Laser welding'; 1999, Toronto, ON, John Wiley & Sons.
6. J. C. Ion: *Sci. Technol. Weld. Join.*, 2000, **5**, (5), 265–276.
7. H. Zhao, D. R. White and T. DebRoy: *Int. Mater. Rev.*, 1999, **44**, (6), 238–266.
8. S. Venkat, C. E. Albright, S. Ramasamy and J. P. Hurley: *Weld. J.*, 1997, **76**, (7), 275s–282s.
9. M. Pastor, H. Zhao, R. P. Martukanitz and T. DebRoy: *Weld. J.*, 1999, **78**, (6), 207s–216s.
10. M. G. Deutsch, A. Punkari, D. C. Weckman and H. W. Kerr: *Sci. Technol. Weld. Join.*, 2003, **8**, (4), 246–256.
11. A. Punkari, D. C. Weckman and H. W. Kerr: *Sci. Technol. Weld. Join.*, 2003, **8**, (4), 269–282.
12. P. W. Fuerschbach: *Weld. J.*, 1998, **77**, (2), 76s–85s.
13. M. Deutsch: 'Effects of Nd:YAG laser welding and VPPAW welding process variables on weld metal geometry and defects of 1.6 mm thick 5182 aluminum', Mater's dissertation, University of Waterloo, Canada, 2002.
14. A. Punkari: 'Variable polarity plasma arc welding and dual-beam Nd:YAG laser welding of aluminum alloys', Master's dissertation, University of Waterloo, Canada, 2002.
15. M. Zhang and S. B. Zhang: US patent no. 5,990,446, 1999.
16. Y. M. Zhang and S. B. Zhang: *Weld. J.*, 1998, **77**, (6), 57–61.
17. Y. M. Zhang and S. B. Zhang: *Weld. J.*, 1999, **78**, (6) 202s–206s.
18. Y. M. Zhang, C. Pan and A. T. Male: *J. Mater. Sci. Lett.*, 2000, **19**, 831–833.
19. Y. M. Zhang, C. Pan and A. T. Male: *Metall. Mater. Trans. A*, 2000, **31A**, 2537–2543.
20. Y. M. Zhang, C. Pan and A. T. Male: *Mater. Sci. Technol.*, 2001, **17**, (10), 1280–1284.

21. Y. M. Zhang, S. B. Zhang and M. Jiang: *Weld. J.*, 2002, **81**, (11), 249s–255s.
22. Y. M. Zhang: Personal communications, University of Kentucky, USA, April 20, 2002.
23. Y. Kwon: 'Double-sided arc welding of AA5182 aluminum alloy sheet', Master's dissertation, University of Waterloo, Canada, 2003.
24. 'ASM handbook', Vol. 2, 'Properties and selection: nonferrous alloys and special purpose materials', 10th edn, 95; 1990, Materials Park, OH, ASM Int.
25. 'ASM handbook', Vol. 6, 'Welding, brazing and soldering'; 1993, Materials Park, OH, ASM Int.
26. W. R. Oates (ed.): 'Welding handbook', Vol. 3, 'Materials and applications', Part 1, 25; 1996, Miami, FL, American Welding Soc.
27. LaserStrobe Model 4Z – Operation Manual, 1999, Control Vision, Idaho Falls, ID, USA.
28. G. F. Vander Voort: 'Metallography principles and practice', 510s, 610s; 1999, Materials Park, OH, ASM Int.
29. D. T. Swift-Hoof and A. E. F. Gick: *Weld. J.*, 1973, **52**, (11), 492s–499s.
30. D. Rosenthal: *Trans. ASME*, 1946, **43**, (11), 849–866.
31. A. A. Wells: *Weld. J.*, 1952, **31**, (5), 263s–267s.
32. P. W. Fuerschbach and G. A. Knorovsky: *Weld. J.*, 1991, **70**, (11), 287s–297s.
33. S. Kou: 'Welding metallurgy', 2nd edn; 2003, Toronto, John Wiley & Sons.
34. C. J. Bailey and A. K. Pilkey: *Mater. Sci. Eng. A*, 2005, **A403**, 1–10.
35. S. Kou and Y. Le: *Metall. Trans. A*, 1988, **19A**, (4), 1075–1082.
36. G. J. Davies and J. G. Garland: *Int. Metall. Rev.*, 1975, **20**, 83–106.
37. H. W. Kerr: Proc. 3rd Int. Conf. on 'Trends in welding research', (ed. S. A. David and J. M. Vitek), Gatlinburg, TN, June 1992, ASM Int., 157–166.
38. J. D. Hunt: *Mater. Sci. Eng.*, 1984, **65**, 75–83.
39. J. Clarke: 'Columnar-to-equiaxed grains transition in gas tungsten arc welds in aluminum-copper alloys', PhD thesis, University of Waterloo, Canada, 1998.
40. J. Clarke, D. C. Weckman and H. W. Kerr: Proc. 5th Int. Conf. on 'Trends in welding research', (ed. J. M. Vitek *et al.*), 72–76; 1999, Materials Park, OH, ASM Int.
41. A. F. Norman, V. Drazhner and P. B. Prangnell: *Mater. Sci. Eng. A*, 1999, **A259**, 53–64.